Spin Berry phase in the Fermi-arc states

Ken-Ichiro Imura[1,2] and Yositake Takane[1]

[1]*Department of Quantum Matter, AdSM, Hiroshima University, Higashi-Hiroshima 739-8530, Japan*

[2]*Kavli Institute for Theoretical Physics, University of California, Santa Barbara, CA 93106, USA*

(Received 14 September 2011; published 12 December 2011)

An unusual electronic property of a Weyl semimetallic nanowire is revealed. Its band dispersion exhibits multiple subbands of partially flat dispersion, originating from the Fermi-arc states. Remarkably, the lowest energy flat subbands bear a finite size energy gap, implying that electrons in the Fermi-arc surface states are susceptible to the spin Berry phase. This is shown to be a consequence of spin-to-surface locking in the surface electronic states. We verify this behavior and the existence of the spin Berry phase in the low-energy effective theory of Fermi-arc surface states on a cylindrical nanowire by deriving the latter from a bulk Weyl Hamiltonian. We point out that in any surface state exhibiting a spin Berry phase π, a zero-energy bound state is formed along a magnetic flux tube of strength $\Phi_0/2 = hc/(2e)$. This effect is highlighted in a surfaceless bulk system pierced by a dislocation line, which shows a 1D chiral mode along the dislocation line.

DOI: 10.1103/PhysRevB.84.245415 PACS number(s): 73.20.−r, 73.63.Fg, 72.25.Mk, 61.72.Lk

I. INTRODUCTION

It has been proposed recently that a three-dimensional (3D) Weyl semimetal phase is likely realized in pyrochlore iridates, $A_2Ir_2O_7$ (A = Y or a lanthanide element).[1] The Weyl semimetal has a unique band structure characterized by a set of discrete linearly dispersive point nodes, the Weyl points.[2–4] Such a band structure of the Weyl semimetal is naturally reminiscent of that of graphene, its 2D counterpart, but unlike 2D Dirac cones as follows: 2D Dirac cones have band structure $H_{2D} = p_x\sigma_x + p_y\sigma_y$, whereas 3D Weyl points have band structure $H_{3D} = p_x\sigma_x + p_y\sigma_y + p_z\sigma_z$. Three-dimensional Weyl points are more stable objects; they cannot be trivially gapped out by a perturbation (cf. H_{2D} is gapped by a local mass term, $H' = m\sigma_z$).

Moreover, unlike topological insulators, the Weyl semimetal is gapless in the bulk, but, when in contact with the vacuum, it exhibits a peculiar surface state, somewhat reminiscent of a more established helical surface state of the topological insulator. The two surface states are indeed both of topological origin, and, in this sense, this analogy between the Weyl semimetal and the topological insulator is not superficial at all. In the bulk (without a surface) the Weyl semimetal is already gapless, but the conduction and the valence bands touch only at discrete points (Weyl points) in the Brillouin zone; let us assume hereafter that there exists only a pair of such point nodes for simplicity. In the presence of a surface, an additional state appears, localized on the surface, and "enveloping" the two point nodes. If one considers the $E = 0$ cross section of the energy spectrum, this additional surface state appears as a line, not necessarily straight but always connecting the two Weyl points, and forms a Fermi arc.[1,2,5–8] As is typically the case with the helical Dirac cone surface state of a topological insulator, the existence of this Fermi-arc envelope state is *topologically* protected by a bulk topological invariant through the so-called bulk/surface correspondence.

As we mentioned earlier, the Weyl semimetal can be regarded as a 3D version of graphene. Such an analogy in the low-energy electronic property of the *bulk* is naturally extended to that of the *surface*. The Fermi-arc state is indeed shown to be a precise 3D analog of the edge states of a graphene nanoribbon in the zigzag edge geometry.[9] These two examples constitute prototypical classes of the topologically nontrivial *gapless* states, which are counterparts of the *gapped* topological insulator and superconductors, the latter known to be classified into the form of a periodic table (tenfold) in terms of their symmetry and dimension.[10–12]

The idea of characterizing topologically nontrivial gapless or nodal states in terms of the topological invariants has been introduced and extensively used in the study of ^{3}He-A.[3,13–15] More recently, it has been applied to the description of topologically nontrivial nodal superconductors.[16–22] A periodic table analogous to the one used for classifying various classes of topological insulators and superconductors has been also proposed for those classes of topologically nontrivial gapless states.[23]

The edge/surface state of a topological insulator is often referred to be "helical," indicating that its spin direction is locked with respect to its propagating direction. Here, in this work we focus on still another unique property of such a helical surface state, i.e., the existence of the spin Berry phase. The electronic spin in the surface helical state shows "spin-to-surface locking,"[24–29] i.e., the spin is locked in plane to the tangential surface of the real space geometry (e.g., on a cylindrical surface). A mathematical description of this spin-to-surface locking, the spin Berry phase, primarily manifests in the finite-size energy gap associated with the surface helical states.[29] In an infinitely large (or doubly periodic) slab geometry, the finite-size energy gap of the surface state due to a finite thickness of the slab decays exponentially as a function of the thickness. In the case of a rectangular/cylindrical nanowire, i.e., when the width of the slab becomes finite, and the slab acquires side surfaces, this is no longer the case. The phase information of the electronic wave function on one surface can be transmitted to that of the opposite surface via the (gapless) side surface states. The finite-size energy gap then decays only algebraically as a function of the thickness. The spin Berry phase replaces the periodic boundary condition applied to the electronic motion around the cylinder by an antiperiodic boundary condition, leading to half-integer quantization of the orbital angular momentum around the cylinder.[29] Such

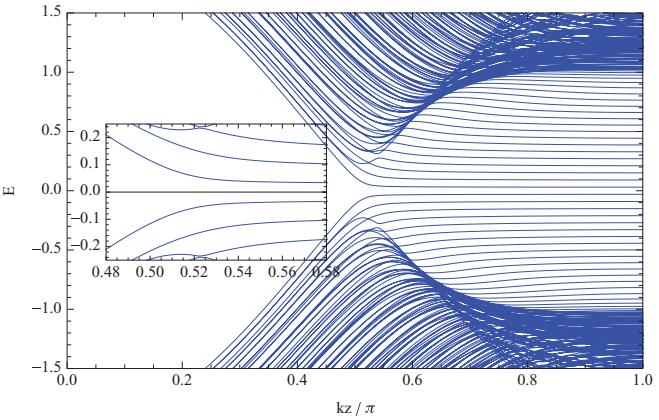

FIG. 1. (Color online) Multiple subbands, originating from a pair of Fermi-arc states connecting the two Weyl points ($k_z = \pm k_0 = \pm\pi/2$) via the Brillouin zone boundary. The subbands have a flat band dispersion, filling the bulk energy gap at $k_z > k_0$. $A = B = t_z = 1$. The simulation is done for a system of square lattice of size, $(N_x, N_y) = (24,24)$, periodic in the z direction. The inset shows details of the spectrum around $k_z = k_0$ and $E = 0$.

an energy-gap due to phase coherent motion of an electron around the (cylindrical) surface is sensitive to introduction of a π-flux tube piercing the nanowire. The sensitivity to π flux is a fingerprint of the existence of a spin Berry phase, which might be directly triggered experimentally in an Aharonov-Bohm-type measurement recently performed in a system of topological insulator nanowires.[30]

As mentioned earlier, the Fermi-arc states resemble the edge states of a zigzag graphene nanoribbon from the viewpoint of topological classification. But still, as we demonstrate in this paper, the Fermi-arc states exhibit, unlike a 2D graphene layer, a specific spin Berry phase. In this regard the Fermi-arc states show a stronger resemblance to the helical surface states of a 3D topological insulator. This paper reveals smoking-gun features of such a spin Berry phase in the Fermi-arc states. We, first, demonstrate in Sec. II that in a nanowire geometry electrons in the Fermi-arc surface states show multiple subbands of a partially flat dispersion (see Fig. 1), but they are susceptible to a finite-size energy gap associated with the spin Berry phase. We then confirm in Sec. III the existence of this spin Berry phase in the surface effective Hamiltonian by deriving it from the bulk effective Hamiltonian. In Secs. IV and V we analyze the system's response to an Aharonov-Bohm flux as well as to introduction of a screw dislocation, confirming the existence of a spin Berry phase. We set $\hbar = 1$, unless otherwise noted.

II. MULTIPLE FLAT SUBBANDS

Let us consider a simple model of a Weyl semimetal with a single pair of Weyl nodes on the k_z axis as follows:[7,8]

$$H = A(k_x\sigma_x + k_y\sigma_y) + M(\boldsymbol{k})\sigma_z, \tag{1}$$

where $\boldsymbol{k} = (k_x,k_y,k_z)$,

$$M(\boldsymbol{k}) = \Delta(k_z) + B\left(k_x^2 + k_y^2\right), \tag{2}$$

and we choose

$$\Delta(k_z) = 2t_z(\cos k_z - \cos k_0). \tag{3}$$

This is a long-wavelength effective Hamiltonian regarding the motion in the x and y directions, whereas, in the z direction, it can be regarded as a tight-binding Hamiltonian. Or, by making the replacements:

$$\begin{aligned} k_x &\to \sin k_x, \\ k_y &\to \sin k_y, \\ k_x^2 &\to 2(1 - \cos k_x), \\ k_y^2 &\to 2(1 - \cos k_y), \end{aligned} \tag{4}$$

the same model can be viewed as a 3D square-lattice tight-binding model. We will employ this square-lattice implementation for numerical simulations.

The energy spectrum of this effective Weyl model is characterized by a pair of Weyl points at $\boldsymbol{k} = (0,0,\pm k_0)$, exhibiting a conic dispersion around them. In addition, a pair of Fermi-arc states appear[1,2,5–8] when we put this system into a slab, say, bounded by two surfaces, one at $x = 0$ and the other as $x = L_x$, parallel to the z axis. Let us fix the parameters such that $t_z > 0$, $B > 0$. Then, for $-k_0 < k_z < k_0$, $\Delta(k_z) > 0$, i.e., $\Delta(k_z)/B > 0$. This means that a cross section of Eq. (1) at a fixed k_z in the above range describes a trivial 2D band insulator. Whereas for $k_0 < k_z < \pi$ and $-\pi < k_z < -k_0$, $\Delta(k_z) < 0$, i.e., $\Delta(k_z)/B < 0$. Then, a similar cross section of Eq. (1) at k_z in one of these ranges describes a topological (quantized anomalous Hall) insulator with a chiral edge mode. There appears one single chiral branch on the $x = 0$ side and another on the $x = L_x$ side, propagating in opposite directions; $-\hat{\boldsymbol{y}}$ and $+\hat{\boldsymbol{y}}$, respectively. These chiral modes show a linear dispersion, therefore, of opposite sign and cross at $k_y = 0$ and at $E = 0$, forming an X-shaped dispersion, $E = E(k_y)$. If one allows k_z to vary continuously, then the locus of such an X-shaped dispersion forms two planar membranes in the (k_y,k_z,E) space, always crossing at $k_y = 0$ (on the k_z axis) and at $E = 0$. The locus of the crossing point is the Fermi arc, connecting the two Weyl points $k_z = k_0$ and $k_z = -k_0$ via the zone boundary. Both ends of the two planar membranes are closed by half-conic structures which appear "beyond" the Weyl points, $k_z < k_0$ and $-k_0 < k_z$. The entire manifold thus formed envelops the two Weyl cone regions.

Let us then further restrict the system into a nanowire geometry; the system is restricted not only between $x = 0$ and $x = L_x$ but also between $y = 0$ and $y = L_y$. The energy spectrum $E = E(k_z)$ of such a Weyl semimetallic nanowire is shown in Fig. 1. The spectrum shows a series of flat subbands as follows:

$$E(k_z) = E_{\pm1}, E_{\pm2}, E_{\pm3}, \ldots, \tag{5}$$

which are remnants of the two planar regions of the Fermi-arc manifold. The flatness of the subbands stems from the fact that the membrane state has no dispersion in the k_z direction. These multiple subbands form *circular chiral modes*, carrying a spontaneous persistent current around the surface of the wire. Note that such circular chiral modes do not appear if one considers a wire perpendicular to the z axis. In that case Fermi-arc type surface states do appear on the surface

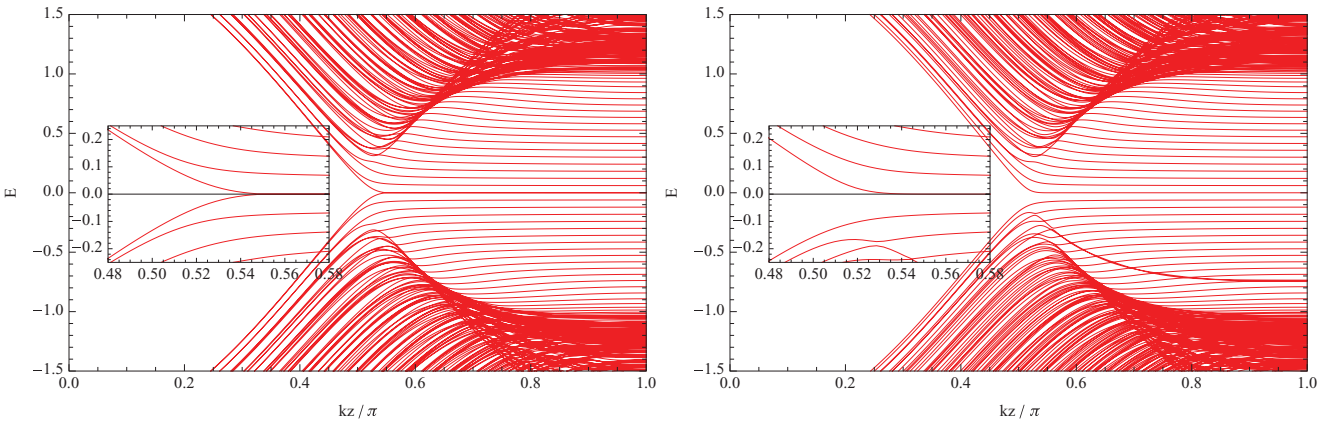

FIG. 2. (Color online) Behavior of multiple flat subbands in the presence of a flux tube $\Phi = \Phi_0/2 = hc/(2e)$ [$\Phi_0 = hc/e$] penetrating the nanowire. (Left) The total flux tube $\Phi = \Phi_0/2$ pierces a single plaquette at each layer. (Right) The flux tube is split into two, each carrying $\Phi/2 = \Phi_0/4$ in order to avoid a zero-energy state bound to the flux tube. $N_x = N_y = 24$.

parallel to the z axis, but they disappear on the side normal to the z axis. Therefore, the surface states cannot completely wrap the wire. This is in marked contras to the topological insulator surface states. The latter, protected by the "strong" bulk/edge correspondence, appear irrespectively of the shape and direction of the surface and, consequently, cover the entire surface. Here, the Fermi-arc subbands are indeed in one-to-one correspondence with the structure of Weyl points in the bulk spectrum. This correspondence is, however, "weak" in the sense that it depends on the direction of the surface. As we mentioned earlier, both the existence and flatness of the Fermi-arc subbands are also topologically protected.

What might be counterintuitive in Fig. 1 is that the lowest conduction and the highest valence subbands, $E_{\pm 1}(k_z)$, are still separated by a finite-size energy gap (see its inset). We see later (Fig. 2, upper panel) that one can actually close this gap by introducing a flux π penetrating the cylinder. In the light of our knowledge on the helical surface states of a 3D topological insulator,[24–29] such a behavior may be naturally attributed to the existence of a spin Berry phase.

Let us come back to Fig. 1 and look into the subband spectra. On the $k_z < k_0$ side, the behavior of $E(k_z)$ directly results from the bulk spectrum. Indeed, for $\Delta(k_z)/B > 0$, only bulk solutions are possible. The "bulk" solutions are the solutions of Eqs. (1), (2), and (3) satisfying the following boundary condition:

$$\psi(0,y) = \psi(L_x,y) = \psi(x,0) = \psi(x,L_y) = \begin{bmatrix} 0 \\ 0 \end{bmatrix}. \quad (6)$$

The "plane-wave" solutions of Eqs. (1), (2), and (3) are

$$|\boldsymbol{k}\pm\rangle_{\text{plane}} = e^{i(k_x x + k_y y)}|k_z\rangle|\boldsymbol{d}(\boldsymbol{k})\pm\rangle, \quad (7)$$

where $\boldsymbol{k} = (k_x,k_y,k_z)$ and $|k_z\rangle$ is a Bloch state with a crystal momentum k_z in the z direction. $|\boldsymbol{d}(\boldsymbol{k})\pm\rangle$ represents a spin state pointing in the direction of $\boldsymbol{d}(\boldsymbol{k}) = [Ak_x, Ak_y, M(\boldsymbol{k})]$, either parallel or antiparallel, depending on the index $\pm$. The plane-wave solution [Eq. (7)] has an energy eigenvalue,

$$E(\boldsymbol{k}) = \pm\sqrt{A^2\left(k_x^2 + k_y^2\right) + M(\boldsymbol{k})^2}. \quad (8)$$

For large-enough $\Delta(k_z)$ such that only the third component of $\boldsymbol{d}(\boldsymbol{k})$ dominates, i.e., $\boldsymbol{d}(\boldsymbol{k}) \parallel \hat{\boldsymbol{z}}$, and one can satisfy the boundary condition Eq. (6) by a simple superposition of $|\boldsymbol{k}\pm\rangle$ with $\boldsymbol{k} = (\pm k_x, \pm k_y, k_z)$, i.e.,

$$|\boldsymbol{k}\pm\rangle_{\text{bulk}} \simeq \sin(k_x x)\sin(k_y y)|k_z\rangle|\hat{\boldsymbol{z}}\pm\rangle, \quad (9)$$

where $\boldsymbol{k} = (n_x\pi/L_x, n_y\pi/L_y, k_z)$ with $n_x, n_y = 1,2,\ldots$. Lowest bulk subbands correspond to $(n_x,n_y) = (1,1)$, $(n_x,n_y) = (1,2)$ and $(2,1)$, $(n_x,n_y) = (2,2)$, $(n_x,n_y) = (1,3)$ and $(3,1)$, and so on. In the crossover regime $k_z \sim k_0$, this simple picture is no longer valid, but the subbands may be still classified by these quantum numbers.

On the $k_z > k_0$ side, the Fermi-arc subbands (5) appear in addition to these bulk solutions. The lowest-energy subband solutions in the bulk merge into the Fermi-arc (surface) subbands in the crossover regime. The Fermi-arc subband solutions are solutions of Eqs. (1), (2), and (3) with (6) with k_x and k_y being a complex number. Their wave functions are localized on the surface of the wire. Last but not the least, the Fermi-arc subbands (5) show a flat spectrum, which appear below the bulk solutions, $|E| < |\Delta(k_z)|$, and exist only in the regime: $\Delta(k_z)/B < 0$.

In the next section, we investigate the nature of such surface Fermi-arc solutions. We derive a low-energy effective Hamiltonian which involves only the surface states. It will become clear that the Fermi-arc solutions indeed emerge from the bulk effective Hamiltonian, Eqs. (1), (2), and (3), but, importantly, with the spin Berry phase, which explains the finite-size energy gap which we have seen in Fig. 1.

III. DERIVATION OF THE SPIN BERRY PHASE—THE SURFACE EFFECTIVE HAMILTONIAN

To clarify the nature of the spin Berry phase, we consider here a cylindrical nanowire of radius R extended along the z axis: $x^2 + y^2 \leqslant R$. We start from the same bulk effective Hamiltonian, Eqs. (1), (2), and (3), but, in order to extract relevant information on the surface electronic states, we divide it into two components,[29,31–35] $H = H_\perp + H_\parallel$, where $H_\perp$ ($H_\parallel$) describes electronic motion perpendicular (tangential) to the cylindrical surface. Equations (1), (2), and (3) represent an

effective theory for $k_x, k_y \ll 1$, but there is no restriction on k_z. Here we consider the case $k_z > k_0$ such that $\Delta(k_z)/B < 0$ and expand it as $k_z = k_z^{(0)} + p_z$. Introducing

$$k_r = -i\frac{\partial}{\partial r}, \quad k_\phi = -i\frac{1}{r}\frac{\partial}{\partial \phi}, \tag{10}$$

conjugate to the cylindrical coordinates $r = \sqrt{x^2+y^2}$, $\phi = \arctan\frac{y}{x}$, one can express $H_\perp$ and $H_\parallel$ as

$$\begin{aligned} H_\perp &= H_\perp(k_r) = H|_{k_\phi=0, k_z=k_z^{(0)}}, \\ H_\parallel &= H_\parallel(k_\phi, p_z). \end{aligned} \tag{11}$$

In order to derive the surface effective Hamiltonian, we, first, have to construct a base solution, the Fermi-arc solution in the present case, satisfying the given boundary condition

$$|\psi(r = R, \phi, z)\rangle = \begin{bmatrix} 0 \\ 0 \end{bmatrix}. \tag{12}$$

Such a base solution is found by solving the electron dynamics perpendicular to the surface,

$$H_\perp|\psi_\perp\rangle = E_\perp|\psi_\perp\rangle, \tag{13}$$

where $H_\perp$ reads explicitly

$$H_\perp = \begin{bmatrix} M_\perp & Ak_r e^{-i\phi} \\ Ak_r e^{i\phi} & -M_\perp \end{bmatrix}. \tag{14}$$

Here we have decomposed the mass term into

$$\begin{aligned} M_\perp &\simeq \Delta\left(k_z^{(0)}\right) + Bk_r^2, \\ M_\parallel &= Bk_\phi^2 - 2t_z \sin k_z^{(0)} p_z. \end{aligned} \tag{15}$$

The Laplacian in the cylindrical coordinates has another contribution, $(1/r)\partial/\partial r$. Here, we neglect this first-order derivative term, keeping only the term $\partial^2/\partial r^2$.[29] This is justified when the radius R of the cylinder is sufficiently larger than the penetration depth [κ^{-1}, see Eq. (16)] of the surface state.

We search for solutions of Eq. (13), which has an energy $E_\perp$, in the range $-\Delta(k_z) < E_\perp < \Delta(k_z)$ and takes the following form:

$$|\psi_\perp\rangle \simeq e^{\kappa(r-R)}|E_\perp, \kappa\rangle, \tag{16}$$

where

$$|E_\perp, \kappa\rangle = \begin{bmatrix} E_\perp + M_\perp(\kappa) \\ -i\kappa A e^{i\phi} \end{bmatrix} \tag{17}$$

and $\kappa > 0$. For a given energy $E_\perp$, κ has two positive solutions, $\kappa = \kappa_\pm$, satisfying

$$\begin{aligned} E_\perp^2 &= M_\perp(\kappa)^2 - A^2\kappa^2, \\ M_\perp(\kappa) &= \Delta - B\kappa^2. \end{aligned} \tag{18}$$

Composing a linear combination of these two base solutions, one can construct a hypothetical wave function,

$$|\psi_\perp\rangle = c_1 e^{\kappa_+(r-R)}|E_\perp, \kappa_+\rangle + c_2 e^{\kappa_-(r-R)}|E_\perp, \kappa_-\rangle, \tag{19}$$

which should be matched with the boundary condition (12), i.e.,

$$\det \begin{bmatrix} E_\perp + M_\perp(\kappa_+) & E_\perp + M_\perp(\kappa_-) \\ -i\kappa_+ A e^{i\phi} & -i\kappa_- A e^{i\phi} \end{bmatrix} = 0. \tag{20}$$

Note that the two wave functions $|\psi\rangle$ and $|\psi_\perp\rangle$ are related by $|\psi\rangle = \psi_\parallel(\phi, z)|\psi_\perp\rangle$. Since $\kappa_+ \neq \kappa_-$, the condition (20) simplifies (after some algebra) to

$$E_\perp(\Delta + E_\perp) = 0. \tag{21}$$

Recall that at fixed k_z the Fermi-arc solution appears in the bulk gap: $-\Delta(k_z) < E_\perp < \Delta(k_z)$, i.e., Eq. (21) imposes $E_\perp = 0$. Substituting this back to Eq. (18), one finds $M_\perp = \pm\kappa A$. For $E_\perp = 0$ and $M_\perp = \kappa A$, Eq. (17) becomes

$$|E_\perp = 0, \kappa\rangle = M_\perp \begin{bmatrix} 1 \\ -ie^{i\phi} \end{bmatrix}, \tag{22}$$

and the two solutions for κ become

$$\kappa_\pm = \frac{A \pm \sqrt{A^2 + 4B\Delta}}{2B}, \tag{23}$$

which is consistent with the condition $\kappa_\pm > 0$ (recall that $B\Delta < 0$). The other choice, $M_\perp = -\kappa A$, is not compatible with this requirement.

Thus, the normalized Fermi-arc base solution is found to be

$$|\psi_\perp\rangle = \rho(r)(e^{\kappa_+(r-R)} - e^{\kappa_-(r-R)}) \begin{bmatrix} 1 \\ -ie^{i\phi} \end{bmatrix}, \tag{24}$$

where

$$\rho(r) \simeq \sqrt{\frac{\kappa_+\kappa_-(\kappa_+ + \kappa_-)}{2\pi R}} \frac{e^{\kappa_+(r-R)} - e^{\kappa_-(r-R)}}{|\kappa_+ - \kappa_-|} \tag{25}$$

($\kappa_\pm R \gg 1$ assumed). Equation (24) is a remarkable result, indicating that the surface spin state is

$$|\hat{\phi}-\rangle = \frac{1}{\sqrt{2}} \begin{bmatrix} e^{-i\phi/2} \\ -ie^{i\phi/2} \end{bmatrix}, \tag{26}$$

diagonalizing a spin operator in the direction of $\hat{\phi}$ with an eigenvalue $-\hbar/2$, where $\hat{\phi}$ is a unit vector pointing to the azimuthal direction,

$$\hat{\phi} = \begin{bmatrix} -\sin\phi \\ \cos\phi \end{bmatrix}. \tag{27}$$

The electronic spin in the Fermi-arc state is locked in the direction (anti-) parallel to that of $\hat{\phi}$, and when an electron goes around the cylinder in the anticlockwise direction, it also rotates, following the curved surface of the cylinder, locked in the direction of $-\hat{\phi}$. After a complete 2π rotation, the electron goes back to the original position on the cylinder, the spin also comes back its original state but with an additional phase of π. This may not be clear from Eq. (24), since it is written in the single-valued representation.[29] Yet, information on the double-valuedness of spin is safely encoded in the surface effective Hamiltonian in the form of a spin Berry phase, as we see below. Notice also that here, in contrast to the case of helical surface states of a topological insulator,[36,37] the surface spin state is not helical. It is, rather, "chiral," pointing to the azimuthal direction of the cylinder independently of the value of k_z. The spin direction is locked, indeed, antiparallel to the group velocity of the surface mode. Let us, finally, see such *chiral* spin-to-surface locking leads, indeed, to the appearance of a

spin Berry phase. Using the base solution (24), we calculate the expectation value of

$$H_{\parallel} = \begin{bmatrix} M_{\parallel} & -iAe^{-i\phi}k_{\phi} \\ -iAe^{i\phi}k_{\phi} & -M_{\parallel} \end{bmatrix} \tag{28}$$

to find

$$H_{\rm surf} = \langle \psi_{\perp} | H_{\parallel} | \psi_{\perp} \rangle = \frac{A}{R}\left(-i\frac{\partial}{\partial\phi} + \frac{1}{2}\right). \tag{29}$$

The low-energy electron dynamics along the surface is, thus, determined by the eigenvalue equation

$$H_{\rm surf}\psi_{\parallel}(\phi,z) = E_{\parallel}\psi_{\parallel}(\phi,z), \tag{30}$$

where $\psi_{\parallel}(\phi,z) = e^{ik_{\phi}\phi}e^{ik_z z}$. The periodic boundary condition around the wire,

$$\psi_{\parallel}(\phi + 2\pi, z) = \psi_{\parallel}(\phi, z), \tag{31}$$

requires that k_{ϕ} be an integer. The spin Berry phase term, i.e., factor $1/2$ in Eq. (29), plays, then, the role of shifting the surface electron spectrum by a half of the finite-size energy gap,

$$E_{\rm surf} = \frac{A}{R}\left(k_{\phi} + \frac{1}{2}\right). \tag{32}$$

Recall that the origin of this $1/2$-spin Berry phase term is that the spin in the Fermi-arc surface state is locked in the direction of Eq. (26). This is in marked contrast to the spin state of the bulk solution; see Eqs. (7) and (9). In the crossover regime $k_z \sim k_0$, the bulk spin state $|\boldsymbol{d}\pm\rangle$ on the $k_z < k_0$ side evolves into the locked surface spin state, Eq. (26). In parallel with this evolution in spin space, the wave function of lowest energy bulk subbands tend to become localized around the boundary. In spectrum, they merge into the Fermi-arc (surface) subbands.

IV. NUMERICAL CONFIRMATION OF THE SPIN BERRY PHASE

Let us verify the existence of a spin Berry phase in numerical experiments. We reconsider the nanowire geometry with a square cross section, which has already appeared in Sec. II. Here, to confirm the existence of the spin Berry phase, we introduce a flux tube Φ piercing the nanowire. In Fig. 2 the energy spectrum in the presence of an infinitely thin π-flux tube, carrying a magnetic flux $\Phi = \Phi_0/2 = hc/(2e)$, with $\Phi_0 = hc/e$ being the unit flux quantum, is shown for comparison with the spectrum in the absence of flux (Fig. 1). The upper panel of Fig. 2 shows the spectrum when the total flux $\Phi_0/2 = hc/(2e)$ pierces, at each cross section, a *single* plaquette. The obtained spectrum shows a gapless dispersion with doubly degenerate zero-energy states. This behavior is, indeed, in marked contrast to the gapped spectrum of Fig. 1, which is reminiscent of an analogous behavior due to the effect of the spin Berry phase on the surface of a topological insulator.[28] Still, it is not simply explained by the effective surface theory, Eqs. (29), (30), (31), and (32), which we derived in the last section. Notice that in the presence of a flux $\Phi_0/2$ penetrating the cylinder, the surface effective Hamiltonian (29) is replaced by

$$H_{\rm surf} = \frac{A}{R}\left(-i\frac{\partial}{\partial\phi} + \frac{1}{2} - \frac{\Phi}{\Phi_0}\right), \tag{33}$$

resulting in a shift of the spectrum

$$E_{\rm surf}(\Phi) = \frac{A}{R}\left(k_{\phi} + \frac{1}{2} - \frac{\Phi}{\Phi_0}\right). \tag{34}$$

Thus, according to the effective surface electron dynamics, Eqs. (33), (30), (31) and (34), the subband spectra are *uniformly* shifted both for k_{ϕ} positive and negative (or null) integer.

Where, then, does the degenerate $E = 0$ pair come from? The answer to this question is almost obvious if one looks into spatial distribution of the corresponding wave function. As a general consequence of the $1/2$-spin Berry phase term, a series of plaquettes (aligned in the z direction), each penetrated by a π-flux tube, always hosts a zero-energy bound state. (A possibly related effect in a strong topological insulator can be found in Ref. 38). The existence of such a bound state might be clear from Eq. (34). As a crude approximation, one can regard the series of plaquettes which accommodates the π flux as a cylinder of a radius $r_0 \sim 1$ (the lattice constant). Taking into account (though this is irrelevant to the discussion here) that the surface state localized around this cylinder will have an opposite chirality (propagating direction), the effective surface Hamiltonian [Eq. (29)] may be modified to describe such a bound state as

$$H_{\rm bound} = -\frac{A}{r_0}\left(-i\frac{\partial}{\partial\phi} + \frac{1}{2} - \frac{\Phi}{\Phi_0}\right). \tag{35}$$

In Eqs. (33) and (35) the electrons feel the same flux, only the propagating direction is opposite. We may write the corresponding wave function as $\psi_{\parallel}(\phi,z) = e^{in\phi}e^{ik_z z}$, with a quantum number n associated with the orbital motion around the flux tube rather than k_{ϕ} to make a distinction between the two. Equation (34) then becomes,

$$E_{\rm bound}(\Phi) = -\frac{A}{r_0}\left(n + \frac{1}{2} - \frac{\Phi}{\Phi_0}\right). \tag{36}$$

In any case, cancellation of the $1/2$-spin Berry phase term by the π flux implies the existence of a zero-energy bound state. Of course, since $r_0 \sim 1 \ll R$, in the spectrum of Eq. (36) only the $E = 0$ ($n = 0$) state is relevant in the energy scale, A/R, of the finite-size energy gap, cf. Eq. (34), and appears in the window of bulk energy gap. Such a bound state along the flux tube is degenerate with the $E = 0$ subband state of Eq. (32) with $k_{\phi} = 0$ and explains the twofold degeneracy of the $E = 0$ state in Fig. 2.

However, if one's purpose is to see simply the effects of the spin Berry phase, one can avoid this complexity. The lower panel of Fig. 2 shows a spectrum when the system is always pierced by a π-flux tube, with a magnetic flux $\Phi = \Phi_0/2 = hc/(2e)$, but *split into two*; each of the half flux $\Phi/2 = \Phi_0/4 = hc/(4e)$ pierces a different plaquette. One can still assume a bound state along such a half flux tube and estimate its energy. For a cylinder penetrated by a half flux tube, Eq. (36) modifies to

$$E_{\rm bound}(\Phi) \to E_{\rm bound}(\Phi/2) = -\frac{A}{r_0}\left(n + \frac{1}{2} - \frac{\Phi/2}{\Phi_0}\right). \tag{37}$$

Clearly, for $\Phi = \Phi_0/2$ and $r_0 \sim 1 \ll R$, there exists no bound state in the scale of finite-size energy gap A/R. The $n = 0$ bound state is sent to the high-energy spectrum (one can

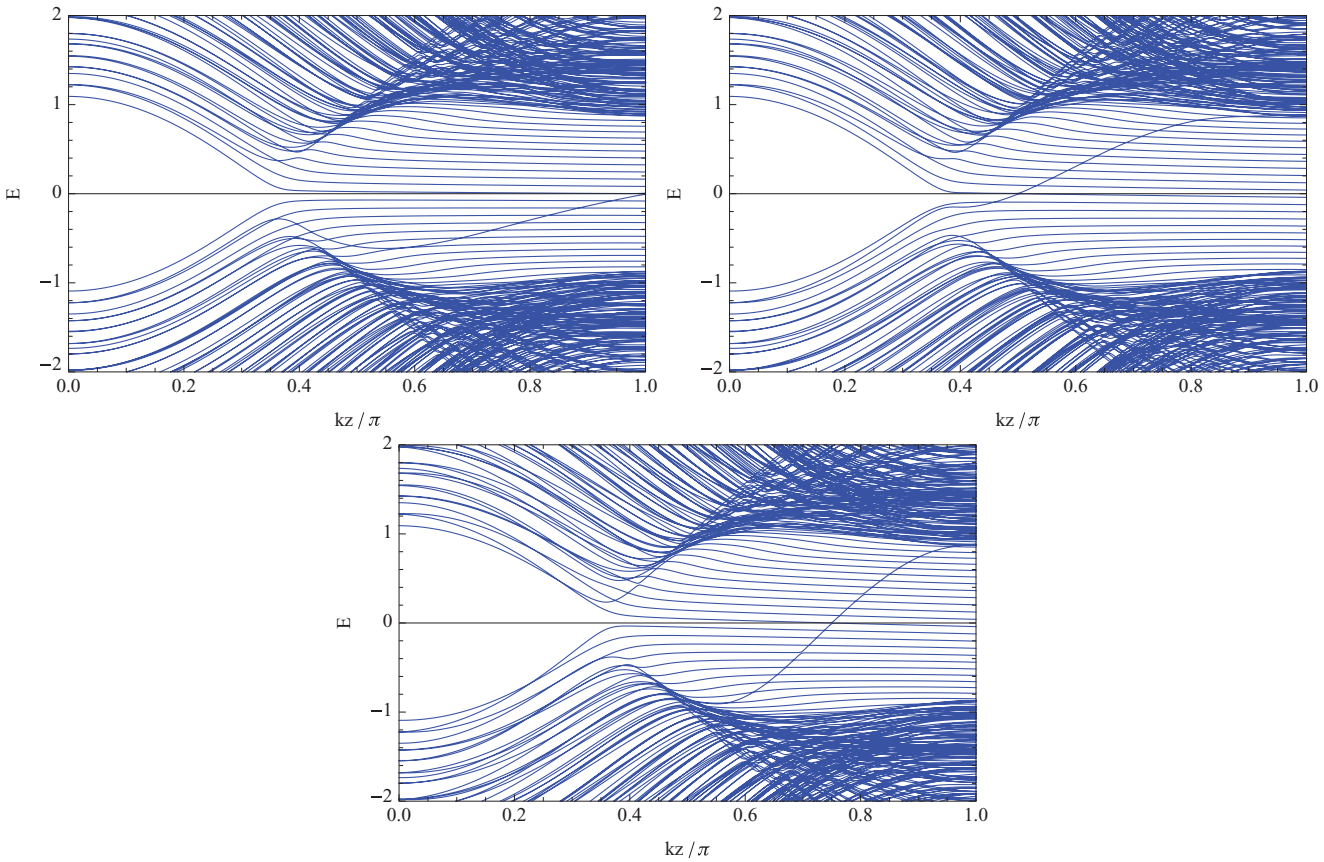

FIG. 3. (Color online) Multiple subbands deformed by a crystal dislocation with a Burgers vector $\boldsymbol{b} = (0,0,b)$, where (upper left) $b = 1$, (upper right) $b = 2$, and (bottom) $b = 4$. $k_0 = \pi/3$, $N_x = N_y = 16$.

actually see this in the lower panel of Fig. 2). Thus, the low-energy (at the energy scale of A/R) spectrum of such a system is simply determined by Eq. (34). The obtained data depicted in the lower panel of Fig. 2 shows behavior consistent with Eq. (34), with a single subband state located precisely at $E = 0$ (see the inset).

An alternative way to verify the existence of the spin Berry phase is to see the system's response to crystal deformation: the introduction of a screw dislocation. A screw dislocation plays, fundamentally, a role similar to the magnetic flux we have considered above,[28,39] but its effect on the subband spectrum superficially differs much more, as shown in Fig. 3. Suppose that the underlying crystal is deformed by a screw dislocation along the axis of the wire (z axis); its Burgers vector is $\boldsymbol{b} = (0,0,b)$ ($b = \pm 1, \pm 2, \ldots$). As opposed to a magnetic flux which twists the phase of an electronic wave function uniformly, a crystal dislocation introduces a phase shift which depends on the crystal momentum k_z, in the direction of the Burgers vector,

$$\psi_{\parallel}(\phi,z) = e^{i[k_\phi - k_z b/(2\pi)]\phi} e^{ik_z z}, \tag{38}$$

introducing a finite slope into the subband spectrum,

$$E_{\text{surf}}(k_z b) = \frac{A}{R}\left(k_\phi + \frac{1}{2} - \frac{k_z b}{2\pi}\right). \tag{39}$$

Notice that the k_ϕ-th subband intersects with the $E = 0$ line at

$$k_z b = (2k_\phi + 1)\pi, \tag{40}$$

similarly to the π-flux case, but this here occurs only at such discrete values of k_z.

Is that all that a dislocation line does to the subband spectrum? No, of course not. In each panel of Fig. 3 one can recognize an isolated mode which has a slope opposite to all the other subband states. This is again due to a bound state formed along a dislocation line. Similarly to the case of a π-flux tube piercing a single plaquette at each (x,y) layer, a series of plaquettes penetrated by the dislocation line may be regarded as a cylinder of radius $r_0 \sim 1$. The spectrum of subband states associated with such a dislocation line reads

$$E_{\text{bound}}(k_z b) = -\frac{A}{r_0}\left(n + \frac{1}{2} - \frac{k_z b}{2\pi}\right). \tag{41}$$

Again, for $r_0 \sim 1$ only at most a few subbands, satisfying a zero-energy condition,

$$k_z b = (2n + 1)\pi, \tag{42}$$

are visible in the relatively small window of the bulk spectrum. Such subbands have a steep positive slope as a function of k_z, opposite to all the other subbands described by Eq. (39) since $R \gg 1$; i.e., the bound state(s) along the dislocation line is (are) propagating modes. Notice that in the two upper panels of Fig. 3 (cases of $b = 1,2$), crossing of the two subbands,

Eqs. (39) and (41), occurs at $k_\phi = n = 0$, whereas in the bottom panel ($b = 4$ case), the same crossing which falls on the Fermi-arc region is at $k_\phi = n = 1$, indicating that $k_z = (3/4)\pi$.

We have seen that a (square cross sectional) cylinder pierced by a dislocation line should be regarded as a pair of concentric cylinders with radii $r_0 \sim 1$ and $R \gg 1$. This allows us to interpret the spectra shown in Fig. 3 as a superposition of two contributions; one from the subbands localized in the vicinity of the outer surface, Eq. (39), and the other from a bound state along a dislocation line, Eq. (41). To double check the validity of such an interpretation in terms of the bound state along a dislocation line, we consider in the next section an extreme example in which only the bound states appear.

V. PROTECTED 1D CHIRAL MODE ALONG A DISLOCATION LINE

Let us, finally, consider a slightly different geometry in which a pair of screw dislocations, one parallel and the other antiparallel with the z axis, penetrates a triply periodic (surfaceless) system; the two dislocation lines are spatially well separated. On a planar region bounded by the two dislocation lines the crystal is dislocated in the z direction by b. This attributes to each dislocation line a pair of Burgers vectors, $\boldsymbol{b} = (0,0,b)$ and $\boldsymbol{b} = (0,0,-b)$. As we have already seen, such a situation is readily described by the cylinder model we have considered in Sec. IV. A minor but not unimportant difference from the previous case is that here the two cylinders are parallel and not concentric. Therefore, on the surface of the two cylinders the orbital motion of an electron around the cylinder is in the same anticlockwise direction. The low-energy electron dynamics on the surface of the two cylinders are described by the same surface effective Hamiltonian (29). Only the Burgers vector differs and modulates the phase of the electronic wave function in different ways; along each of the dislocation line, Eq. (38) should be replaced by

$$\psi_1(\phi,z) = e^{i(n_1 - k_z b/(2\pi))\phi} e^{ik_z z}, \tag{43}$$

$$\psi_2(\phi,z) = e^{i(n_2 + k_z b/(2\pi))\phi} e^{ik_z z}. \tag{44}$$

The corresponding bound state spectra read

$$E_1(k_z b) = \frac{A}{r_0}\left(n_1 + \frac{1}{2} - \frac{k_z b}{2\pi}\right), \tag{45}$$

$$E_2(k_z b) = \frac{A}{r_0}\left(n_2 + \frac{1}{2} + \frac{k_z b}{2\pi}\right). \tag{46}$$

Again, since $r_0 \sim 1$ only the lowest energy subbands, satisfying the zero-energy condition,

$$k_z b = (2n_1 + 1)\pi, \quad -k_z b = (2n_2 + 1)\pi, \tag{47}$$

are relevant in the spectrum. Some concrete examples of calculated spectra for such a system are shown in Fig. 4 for $b = 1$ (top), $b = 2$ (central), and $b = 4$ (bottom). Each spectrum exhibits a pair of chiral modes, which are identified as the states represented by Eqs. (43) and (44) with n_1 and n_2 satisfying Eqs. (47) in the Fermi-arc region: $k_0 < k_z < \pi$. For

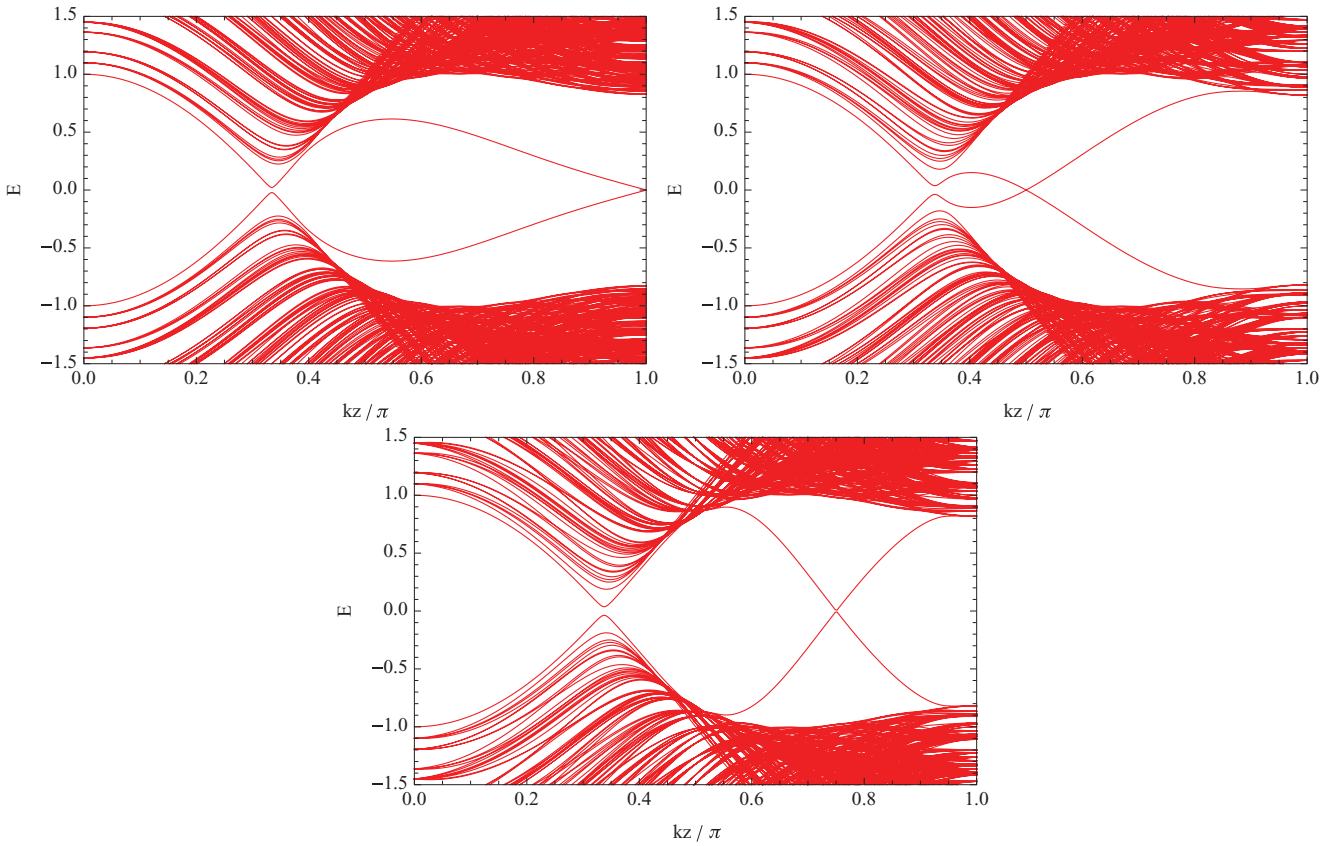

FIG. 4. (Color online) One-dimensional chiral modes along a pair of dislocation lines; $b = 1$ (upper left), $b = 2$ (upper right), and $b = 4$ (bottom). $k_0 = \pi/3$, $N_x = N_y = 24$.

the two upper panels (cases of $b = 1,2$), $n_1 = 0$, $n_2 = -1$, i.e., the two chiral modes intersect at $k_z = \pi/b$ and at $E = 0$. As for the last panel ($b = 4$), $n_1 = 1, n_2 = -2$, indicating that the intersection occurs at $k_z = (3/4)\pi$. Note that this type of gap closing always occurs at $E = 0$ and at the same k_z points uniquely determined by the Burgers vector. Such a feature is model independent and, in this sense, these chiral modes are protected. Notice, in contrast, that projection of the 3D Weyl point onto the 1D Brillouin zone ($k_z = \pi/3$ in Fig. 4) is gapped by the screw dislocation.

It is also interesting that such a pair of zero-energy bound states have a dispersion in the k_z direction; they have a finite group velocity of order $\sim A$ and are propagating along the dislocation line but in the opposite direction on each of the dislocation lines. In this sense we call each of them a 1D *chiral* mode. Note that here the meaning of "chiral" differs from when we used the same word to describe the chiral property of the Fermi-arc surface state or its subbands. Indeed, on each of the dislocation lines the circular orbital motion of an electron in the Fermi-arc state (around a hypothetical cylinder of radius $r_0 \sim 1$) is in the same anticlockwise direction but follows a spiral which evolves in the opposite direction ($+z$ or $-z$), reflecting the opposite direction of the Burgers vector.

VI. CONCLUSIONS

We have studied electronic states of a 3D Weyl semimetal, which serve, in this regard, as the 3D counterparts of graphene. Naturally, the corresponding Fermi-arc surface states could be regarded as a 2D version of 1D edge modes with a flat dispersion, which are known to exist in the zigzag edge nanoribbon.

This paper, however, points out a crucial difference between the two systems. The Fermi-arc surface states exhibit a specific type of (chiral) spin-to-surface locking. This manifests as a spin Berry phase when one considers a curved surface, e.g., a cylindrical surface. In 1D edge states of the zigzag nanoribbon the edge pseudospin state is determined rather by the structure of the edge.[40,41] The spin Berry phase has been regarded as a hallmark property of the helical surface states of a topological insulator. In this paper we have demonstrated that in the case of 3D Weyl semimetal, the existence of peculiar spin Berry phase in the Fermi-arc state leads to a number of unusual finite-size effects: (i) The nanowire spectrum shows a feature of multiple subbands, which is gapped at $E = 0$ (at the level of Weyl points), and (ii) in the case of triply periodic surfaceless system, a protected gapless chiral mode appears along a dislocation line and dominates the low-energy transport.

As a general remark, we have emphasized that whenever a system bears a surface state involving a spin Berry phase, a series of plaquettes pierced by a π-flux tube always hosts a zero-energy bound state. The second statement above is a specific version of this general phenomenon in the case of a 3D Weyl semimetal bearing Fermi-arc states.

ACKNOWLEDGMENTS

K.I. acknowledges Y. B. Kim and A. Schnyder for useful discussions. The authors are supported by KAKENHI; K.I. was supported by the "Topological Quantum Phenomena" (Grant No. 23103511), and Y.T. by a Grant-in-Aid for Scientific Research (C) (Grant No. 21540389). K.I. was also supported in part by the National Science Foundation under Grant No. NSF PHY05-51164.

[1] X. Wan, A. M. Turner, A. Vishwanath, and S. Y. Savrasov, Phys. Rev. B **83**, 205101 (2011).
[2] L. Balents, Physics **4**, 36 (2011).
[3] G. E. Volovik, *The Universe in a Helium Droplet* (Oxford University Press, Oxford, UK, 2003).
[4] S. Murakami, New J. Phys. **9**, 356 (2007).
[5] W. Witczak-Krempa and Y. B. Kim, (2011) e-print arXiv:1105.6108 [cond-mat.str-el].
[6] G. Xu, H. Weng, Z. Wang, X. Dai, and Z. Fang, Phys. Rev. Lett. **107**, 186806 (2011).
[7] K.-Y. Yang, Y.-M. Lu, and Y. Ran, Phys. Rev. B **84**, 075129 (2011).
[8] A. A. Burkov and L. Balents, Phys. Rev. Lett. **107**, 127205 (2011).
[9] M. Fujita, K. Wakabayashi, K. Nakada, and K. Kusakabe, J. Phys. Soc. Jpn. **65**, 1920 (1996).
[10] A. P. Schnyder, S. Ryu, A. Furusaki, and A. W. W. Ludwig, Phys. Rev. B **78**, 195125 (2008).
[11] S. Ryu, A. P. Schnyder, A. Furusaki, and A. W. W. Ludwig, New J. Phys. **12**, 065010 (2010).
[12] A. Y. Kitaev, in *Advances in Theoretical Physics*, edited by V. Lebedev and M. Feigel'man, AIP Conf. Proc. No. 1134 (AIP, Melville, NY, 2009), p. 22.
[13] G. E. Volovik, *Exotic Properties of Superfluid ^{3}He* (World Scientific, Singapore, 1992).
[14] T. T. Heikkilä, N. B. Kopnin, and G. E. Volovik, Sov. J. Exp. Theor. Phys. Lett. **94**, 233 (2011).
[15] Y. Tsutsumi, M. Ichioka, and K. Machida, Phys. Rev. B **83**, 094510 (2011).
[16] M. Sato, Phys. Rev. B **73**, 214502 (2006).
[17] M. Sato and S. Fujimoto, Phys. Rev. B **79**, 094504 (2009).
[18] K. Yada, M. Sato, Y. Tanaka, and T. Yokoyama, Phys. Rev. B **83**, 064505 (2011).
[19] S. Sasaki, M. Kriener, K. Segawa, K. Yada, Y. Tanaka, M. Sato, and Y. Ando, Phys. Rev. Lett. **107**, 217001 (2011).
[20] A. P. Schnyder and S. Ryu, Phys. Rev. B **84**, 060504 (2011).
[21] P. M. R. Brydon, A. P. Schnyder, and C. Timm, Phys. Rev. B **84**, 020501 (2011).
[22] A. P. Schnyder, P. M. R. Brydon, and C. Timm, (2011), e-print arXiv:1111.1207 [cond-mat.supr-con].
[23] S. Ryu, in *Workshop and School on Topological Aspects on Condensed Matter Physics", ICTP, Trieste, 27 June–8 July*; A. Schnyder, in *Fifth Stig Lundqvist Conference on the Advancing Frontiers of Condensed Matter Physics, ICTP, Trieste, 11–15 July, 2011*.
[24] Y. Zhang, Y. Ran, and A. Vishwanath, Phys. Rev. B **79**, 245331 (2009).
[25] Y. Zhang and A. Vishwanath, Phys. Rev. Lett. **105**, 206601 (2010).
[26] P. M. Ostrovsky, I. V. Gornyi, and A. D. Mirlin, Phys. Rev. Lett. **105**, 036803 (2010).

[27]J. H. Bardarson, P. W. Brouwer, and J. E. Moore, Phys. Rev. Lett. **105**, 156803 (2010).
[28]K.-I. Imura, Y. Takane, and A. Tanaka, Phys. Rev. B **84**, 035443 (2011).
[29]K.-I. Imura, Y. Takane, and A. Tanaka, Phys. Rev. B **84**, 195406 (2011).
[30]H. Peng, K. Lai, D. Kong, S. Meister, Y. Chen, X.-L. Qi, S.-C. Zhang, Z.-X. Shen, and Y. Cui, Nat. Mater. **9**, 225 (2010).
[31]H. Zhang, C.-X. Liu, X.-L. Qi, X. Dai, Z. Fang, and S.-C. Zhang, Nat. Phys. **5**, 438 (2010).
[32]C.-X. Liu, X.-L. Qi, H. Zhang, X. Dai, Z. Fang, and S.-C. Zhang, Phys. Rev. B **82**, 045122 (2010).
[33]W.-Y. Shan, H.-Z. Lu, and S.-Q. Shen, New J. Phys. **12**, 043048 (2010).
[34]B. Zhou, H.-Z. Lu, R.-L. Chu, S.-Q. Shen, and Q. Niu, Phys. Rev. Lett. **101**, 246807 (2008).
[35]K.-I. Imura, A. Yamakage, S. Mao, A. Hotta, and Y. Kuramoto, Phys. Rev. B **82**, 085118 (2010).
[36]D. Hsieh *et al.*, Nature **460**, 1101 (2009).
[37]M. Z. Hasan and C. L. Kane, Rev. Mod. Phys. **82**, 3045 (2010).
[38]G. Rosenberg, H.-M. Guo, and M. Franz, Phys. Rev. B **82**, 041104 (2010).
[39]Y. Ran, Y. Zhang, and A. Vishwanath, Nat. Phys. **5**, 298 (2009).
[40]A. H. Castro Neto, F. Guinea, N. M. R. Peres, K. S. Novoselov, and A. K. Geim, Rev. Mod. Phys. **81**, 109 (2009).
[41]Y. Shimomura, Y. Takane, and K. Wakabayashi, J. Phys. Soc. Jpn. **80**, 054710 (2011).